

## Validation of Maritime Rainfall Retrievals from the TRMM Microwave Radiometer

MIN-JEONG KIM, JAMES A. WEINMAN, AND ROBERT A. HOUZE

*Department of Atmospheric Sciences, University of Washington, Seattle, Washington*

(Manuscript received 25 April 2003, in final form 31 December 2003)

### ABSTRACT

This study compares the surface rainfall retrieved from the Goddard profiling (GPROF; version 5) algorithm with Kwajalein ground-based radar (KR) observations at 0.1°, 0.25°, and 1° resolutions. Comparisons of the GPROF-retrieved rainfall with KR observations for 178 overpasses show that GPROF overestimated surface rainfall with respect to the KR by 16%. Power spectral density comparisons between GPROF and KR rain maps at 0.1° resolution show that GPROF-retrieved rain maps are less spatially variable at wavelengths less than 50 km in the mean, suggesting that GPROF rainy areas are smoother and more spatially extensive than those observed by the KR. Sensitivity of rainfall retrievals to the melting layer and the impact of 85-GHz channels were tested. This study introduced Klaassen's melting-layer parameterization into the GPROF algorithm that reduced the GPROF-retrieved rainfall amount by 7.5%. Considering the poor correlation between upper-level ice amounts and surface rainfall, this study only estimated the convective area fraction from 85-GHz brightness temperature and neglected 85-GHz brightness temperature in the rainfall retrieval. This modification reduced GPROF-retrieved surface rainfall amount by 3.5% and made the GPROF-retrieved rainfall retrievals more consistent with the KR observations where the GPROF algorithm overestimated surface rainfall with respect to the KR because of strong ice scattering. For the 178 overpasses used in this study the total rainfall amount retrieved by the revised GPROF algorithm overestimated rainfall by 1% with respect to that measured by the KR.

### 1. Introduction

Three-fourths of the energy that drives atmospheric circulation is latent heat released by precipitation (Sellers 1965; Hartmann 1994). Despite its importance, precipitation is one of the most difficult atmospheric parameters to measure because of large variability in space and time. It is especially difficult to measure precipitation over oceans because surface-based observations such as radars and rain gauges are rare. The shortage of rainfall observations over oceans has been an obstacle for atmospheric research. Rainfall measurements from space offer a solution to this limitation.

Numerous infrared and passive microwave techniques using satellite data have yielded diverse rain estimates to fulfill this demand for the past several decades (Wilheit et al. 1977; Kummerow and Weinman 1988; Spencer et al. 1989; Petty and Katsaros 1990; Smith et al. 1992; Adler and Negri 1988). However, because of limitations such as the sensor's footprint size and insufficient sampling, the satellite rain products were made mainly at a coarse resolution (1° or coarser) for the purpose of large-scale atmospheric research. Providing

high-resolution rainfall products for mesoscale atmospheric research has also been a concern of the satellite remote sensing community.

The Tropical Rainfall Measuring Mission (TRMM) satellite was designed to address this need. It has a nonsynchronous orbit with a low altitude (350 and 402.5 km before and after changing the altitude between 7 and 20 August 2001) and low inclination (35°). Instruments on the TRMM satellite include the TRMM Microwave Imager (TMI) and the precipitation radar (PR). The TMI, on which this study focused, is a nine-channel passive microwave radiometer whose characteristics are summarized in Kummerow et al. (1998). The TMI has much bigger footprint sizes than the TRMM PR (4.3 km), but the swath width of the TMI is 3 times that of the PR, such that the TMI provides better sampling. Moreover, the TMI provides information about the frozen hydrometeors in the upper levels of the cloud because 85-GHz channels of microwave radiometers are sensitive to ice scattering while it is somewhat more difficult to tell the phase of hydrometeors with the total reflectivity measured by the PR.

In addition to these characteristics, the possibility of linking TMI to other radiometers is an advantage because several satelliteborne radiometers, with additional channels and resolutions similar to that of the TMI, currently exist or are planned to be launched in the

---

*Corresponding author address:* Min-Jeong Kim, Department of Atmospheric Sciences, University of Washington, Box 351640, Seattle, WA 98195.  
E-mail: mjkim@atmos.washington.edu

future. For example, the *Aqua* satellite carrying the Advanced Microwave Scanning Radiometer for the Earth Observing System (AMSR-E) was launched in May 2002. A similar radiometer carried aboard the Japanese *Advanced Earth Observing Satellite-II (ADEOS-II)* was launched in December 2002. In addition, the National Polar-Orbiting Operational Environmental Satellite System (NPOESS) and the Global Precipitation Measurement (GPM), which is a follow-on and expanded mission of TRMM, will launch satellites carrying radiometers somewhat similar to the TMI after 2007.

Microwave rainfall retrieval algorithms using satellite-measured brightness temperatures are generally based on empirical or physical methods. Empirical methods calculate a regression to find the relation between observed radiances and ground-based rainfall measurements. They are simple to calculate, easy to implement, and errors can be quantified easily, although their applicability beyond the validation site may be questionable (Kummerow 1998).

Physical methods employ a radiative transfer model to calculate brightness temperatures at the top of the atmosphere at specified rain rates (Weinman and Guetter 1977; Wilheit et al. 1977; Wu and Weinman 1984; Smith and Mugnai 1988; Kummerow and Weinman 1988). As an example, the TMI rainfall retrieval algorithm, referred to as the Goddard profiling (GPROF) algorithm, employs the cloud radiative simulations from the Goddard Cumulus Ensemble (GCE) model to save computational time and to provide guidance for the vertical distribution of radiatively active atmospheric constituents. The model has been run for a variety of tropical soundings to produce simulated hydrometeor profiles. Using vertical profiles of the atmosphere (temperature, humidity, and surface wind) and the simulated hydrometeor profiles for cloud liquid, cloud ice, rain, snow, graupel, and hail provided by this cloud model, brightness temperatures are calculated by the Eddington radiative transfer model (Wu and Weinman 1984). These calculated brightness temperatures and cloud profiles are averaged over areas that are commensurate with the field of view of TMI at 85 GHz. These averaged brightness temperatures, hydrometeor profiles, and convective area fractions are stored in a lookup table, which is referred to as the GPROF database. With brightness temperatures from the TMI, the GPROF algorithm generates the best-fit hydrometeor profiles by employing a probability method based on Bayesian theory that minimizes the difference between observations and profiles stored in the GPROF database (Kummerow et al. 2001). The Bayesian algorithm allows for an internal calculation of the random error of estimates due to the lack of specific information in the observations. In addition to brightness temperatures, the convective area fraction, which is deduced from the TMI-measured brightness temperature pattern (Olson et al. 2001c), is employed in Bayesian calculations as an additional observable. The reason for considering the convective area fraction is to over-

come the beam-filling problem caused by the horizontal inhomogeneity of hydrometeors inside the satellite field of view (Kummerow et al. 2001). The advantage of the physical approach is that each assumption can be individually tested. Realistic error estimates can also be established for each assumption. However, such error tests have been difficult to perform (Kummerow 1998) due to the limited number of observations with which the results can be compared.

By comparing the retrieved rainfall with Kwajalein radar (KR) observations, this study attempts to evaluate the ability of the GPROF algorithm (version 5) to retrieve surface rainfall at 0.1°, 0.25°, and 1.0° resolutions. The data analysis at these resolutions can illuminate the inherent error sources of the algorithm, which can be hidden in coarse-resolution data by averaging. Based on these comparisons, this study shows important factors and their effect on rainfall retrievals. Methods to decrease error sources in the GPROF algorithm are sought and tested by modifying the algorithm to retrieve surface rainfall more consistent with the KR observations.

Section 2 introduces the KR and data processing methods. Section 3 compares GPROF rainfall retrievals and KR observations. Section 4 introduces the melting-layer effect in the GPROF algorithm using Klaassen's (1990) melting-layer parameterization. Section 5 presents the impact of 85-GHz channels on rainfall retrieval. Section 6 presents summary discussion and conclusions.

## 2. Data and methods of analysis

This study focuses on the oceanic GPROF algorithm, so the validation site should be located in the open ocean. Kwajalein Island is an ideal site for this purpose because Kwajalein and neighboring atolls are composed of tiny islands surrounding large lagoons in the open ocean (Fig. 1). The Kwajalein Atoll is in a rainy location on the northern edge of the Pacific intertropical convergence zone (ITCZ) and receives rain from all varieties of oceanic tropical convection. Schumacher and Houze (2003a,b) show that Kwajalein receives not only moderately frequent rain from convective systems with large stratiform rain components, it also has a large population of isolated shallow convection (< ~5 km deep) precipitation. The validation area is defined by the 150-km radius around the radar that is located on Kwajalein Island (8.72°N, 167.73°E). The inner circle in Fig. 1 shows the 15-km range from the KR. The KR data inside of this circle are not used in order to avoid clutter due to radar reflection off the ocean surface.

The KR is a three-dimensionally scanning S-band dual-polarization Doppler weather radar (Schumacher and Houze 2000). The small and largely inaccessible land surface of the Kwajalein Atoll precludes the deployment of a large network of rain gauges. Over land, a network of several hundred rain gauges can serve as a calibration standard (Joss et al. 1998). However, over

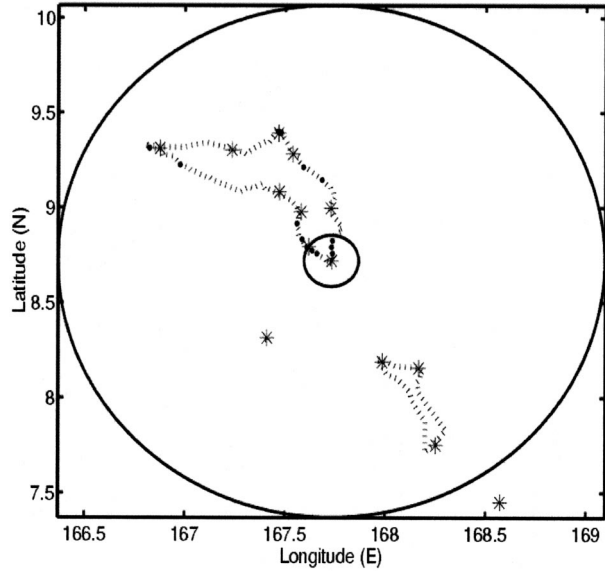


FIG. 1. Map of the Kwajalein area centered on the KR. The geography of the Kwajalein Atoll and neighboring atolls are indicated by dashed lines. Rain gauge locations are indicated by asterisks. The interior of each atoll is a giant lagoon. The inner and outer circles show 15- and 150-km ranges from the KR, respectively.

99% of the Kwajalein validation area surveyed by the radar is ocean and the approximately 5–10 rain gauge–radar pixel pairs usually available from the atoll region are inadequate for statistical calibration. Therefore, the reflectivities of the KR were calibrated using the PR, which is known to have an accuracy of 1 dB (Kummerow et al. 1998; Kozu et al. 2001), by the Mesoscale Group at the University of Washington (UW). The calibration algorithm determines a calibration correction by seeking the dBZ correction required to make the area covered by echo seen by the KR at reflectivity >17 dBZ (sensitivity of the PR) at the 6-km level (ice region), which most closely matches the area of echo >17 dBZ with the reflectivity seen by the PR 2A25 (three-dimensional-gridded attenuation-corrected reflectivity; Iguchi et al. 2000) at the same level. The 6-km level was chosen because it lies above the melting layer and above strong convective cores so that they are not subject to attenuation and they are sufficiently far below the echo top that the sample size is reasonable. The radar reflectivity–rainfall ( $Z$ – $R$ ) relationship,  $Z = 175R^{1.5}$ , was obtained by examining the disdrometer data collected in the 1999 and 2000 wet seasons (Houze et al. 2003). The KR rain products are created operationally at 2-km horizontal resolution. A conservative estimate of typical hardware calibration uncertainty at Kwajalein is ~2 dB, and this uncertainty is estimated to cause  $\pm 30\%$  uncertainty in rain rate calculated from the  $Z$ – $R$  relation (Houze et al. 2003). Considering the inability of the radar to measure reflectivity below the lowest beam and the uncertainty of the drop size distribution measurements, the total uncertainty is even bigger. The sources

of discrepancy between KR data calibrated by the UW and the National Aeronautics and Space Administration (NASA) Goddard Space Flight Center (GSFC) are still in debate; however, this study uses the KR data calibrated by UW to compare with GPROF-retrieved rainfall products. A comprehensive description of rain map products and the sources of uncertainty are found in Houze et al. (2004).

The number of pixels per scan of the 10.65-, 19.35-, 21.3-, and 37-GHz channels is 104. The 85-GHz channels provide 2 times as many pixels (208) as the other channels because of their small footprint size. The effective field of view (Kummerow et al. 1998) in the down track (cross track) is 9.1 (63.2), 9.1 (30.4), 9.1 (22.6), 9.1 (16.0), and 4.6 km (7.2 km) for 10.65-, 19.35-, 21.3-, 37-, and 85-GHz channels, respectively.

The main data used in this study are TMI-measured brightness temperatures, GPROF-retrieved surface rainfall products (Kummerow et al. 2000), and KR-estimated rain rates for 178 TRMM satellite overpasses, which covered the whole validation area and had significant rain (mean rain rate > 1 mm h<sup>-1</sup>) over Kwajalein that occurred between August 1998 and December 2000. Although the KR has been calibrated with the PR, the KR can provide more rain maps coincident with the TMI overpasses than the PR because the KR has better temporal sampling. Rainfall products from the GPROF algorithm have the same horizontal resolution as the TMI 85-GHz channels because the brightness temperatures for all channels are linearly interpolated to the 85-GHz footprint locations, and then the GPROF algorithm is applied to all footprints.

Area-averaged rain rates at 0.1° resolution are calculated with GPROF-retrieved rain rates and 6-km area-averaged KR rain rates. There were no missing values for both the KR and GPROF rain rates inside the validation domain. If a 6-km resolution grid box for the KR is partly outside of the validation domain (Fig. 1), both the KR and GPROF data at 0.1° resolution are dropped as missing values. The KR is calibrated by the PR and the minimum detectable signal of the PR is 17 dBZ (~0.5 mm h<sup>-1</sup>) (Schumacher and Houze 2000). As a consequence, rain rates less than 0.5 mm h<sup>-1</sup> at 0.1° resolution are treated as nonraining both for the GPROF algorithm and KR in this study. By applying 0.5 mm h<sup>-1</sup> nonrain criterion, 6% of the total GPROF rain amount and 3.3% of the total KR rain amount were considered as no rain.

Area-averaged rain rates at 0.25° and 1° resolutions are calculated with those area-averaged rain rates at 0.1° resolution. The total number of pixels available at 0.25° resolution from 178 cases was 14 963, both for the GPROF algorithm and KR. The number of rainy (rain > 0 mm h<sup>-1</sup>) pixels at 0.25° resolution was 5043 for the KR and 4498 for the GPROF algorithm.

The area of the 0.25° grid boxes is commensurate with area of the effective field of view (9.1 km × 63.2 km) of TMI 10.65-GHz channels. [The area of instan-

taneous field of view is  $36 \text{ km} \times 59 \text{ km}$  according to Kummerow et al. (1998)]. Although TMI has a slanting view, which may add location error up to 11 km (Bauer et al. 1998), the information from the 19.35- and 37-GHz emission channels, which have small footprint sizes ( $277$  and  $146 \text{ km}^2$  for 19.35- and 37-GHz channels, respectively) and on which the GPROF algorithm depends most for rainfall retrievals, can compensate for that error if we consider  $0.25^\circ$  resolution as the TMI footprint size. The GPROF rainfall products are created along the scan lines and they depend on the direction of the satellite overpass, while the KR rainfall products are gridded in a latitude–longitude grid. The differences between the grid shapes of the original KR data and GPROF rainfall products are neglected in this study.

### 3. Comparison of rainfall retrieved from the TMI with KR observations

#### a. Rainfall intensity

Figure 2 compares GPROF-retrieved rain rates with KR-estimated rain rates for the 178 cases at  $1^\circ$  and  $0.25^\circ$  resolutions. This figure does not show the points where rain from one or both instruments is zero. For better presentation, the axes have been stretched in the light/moderate rain range by the relation  $X = \text{rain rate}/(\text{rain rate} + A)$ , where  $A$  is 0.5 for  $1^\circ$  resolution and 2 for  $0.25^\circ$  resolution, because the occurrence of light rain rates is greater than occurrences of heavy rain rates. The  $A$  values are chosen at the mode of KR rain-rate occurrences for the 178 cases at  $1^\circ$  and  $0.25^\circ$  resolutions.

The solid lines in Fig. 2 show the 1:1 relation. The result indicates that the GPROF algorithm underestimates (overestimates) rainfall at light (heavy) rain rates when compared with the KR rain rates at  $1^\circ$  resolution. It is hard to tell whether the pattern of the GPROF rain rates is biased with respect to the KR rain rates at  $0.25^\circ$  resolution from this scatterplot. The correlation coefficients between the GPROF and KR rain rates (before converting into  $X$  values) are 0.87 and 0.70 at  $1^\circ$  and  $0.25^\circ$  resolutions, respectively. The points where rain from one or both instruments is zero are included in the correlation coefficient calculations. In Kummerow et al. (2001), an alternative rainfall estimate was made by the KR, which was calibrated by a bulk-adjustment approach to force the radar data into agreement with collocated rain gauges. That study showed that the correlation coefficient at  $1^\circ$  resolution for 1998 overpasses was 0.95.

In order to highlight the bias pattern of GPROF-retrieved rainfall as compared with KR-measured rainfall at each resolution, Fig. 3 presents histograms of the number of rain-rate occurrences for the 178 overpasses. The histograms also show that the GPROF algorithm retrieves rain rates larger than  $13 \text{ mm h}^{-1}$  more often than the KR at  $0.25^\circ$  resolution. Although it is not apparent in Fig. 3, the occurrences of the light rain rates

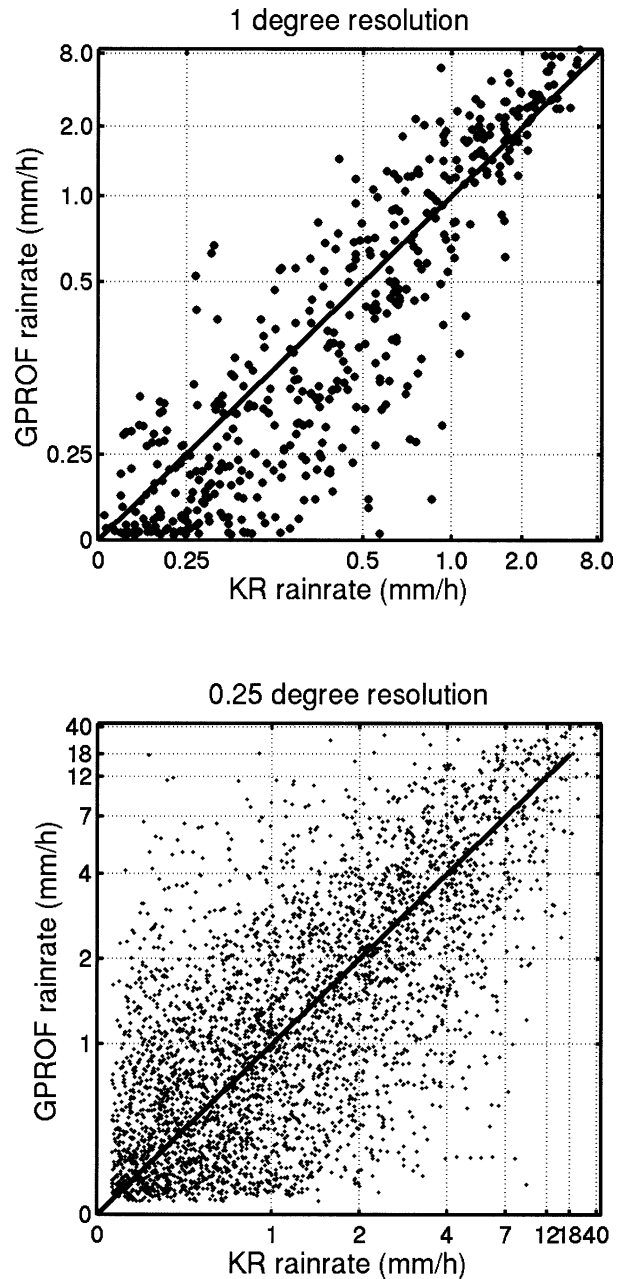


FIG. 2. Scatterplots of GPROF-retrieved and KR-estimated rain rates. Dashed line shows 1:1 relation. Solid lines were calculated by minimizing the least squares differences in both KR and GPROF rain rates.

( $0 \text{ mm h}^{-1} < R \leq 1 \text{ mm h}^{-1}$ ) at  $0.25^\circ$  resolution were less for the GPROF algorithm than for the KR by 20%. This may be caused by the fact that shallow and isolated rain elements, which are known to occur often over the tropical oceans (Schumacher and Houze 2003b), are considered as low rain rates in the KR while the GPROF algorithm may miss them. The distribution of rainfall occurrences of the GPROF algorithm and KR are generally consistent with each other at rain rates between

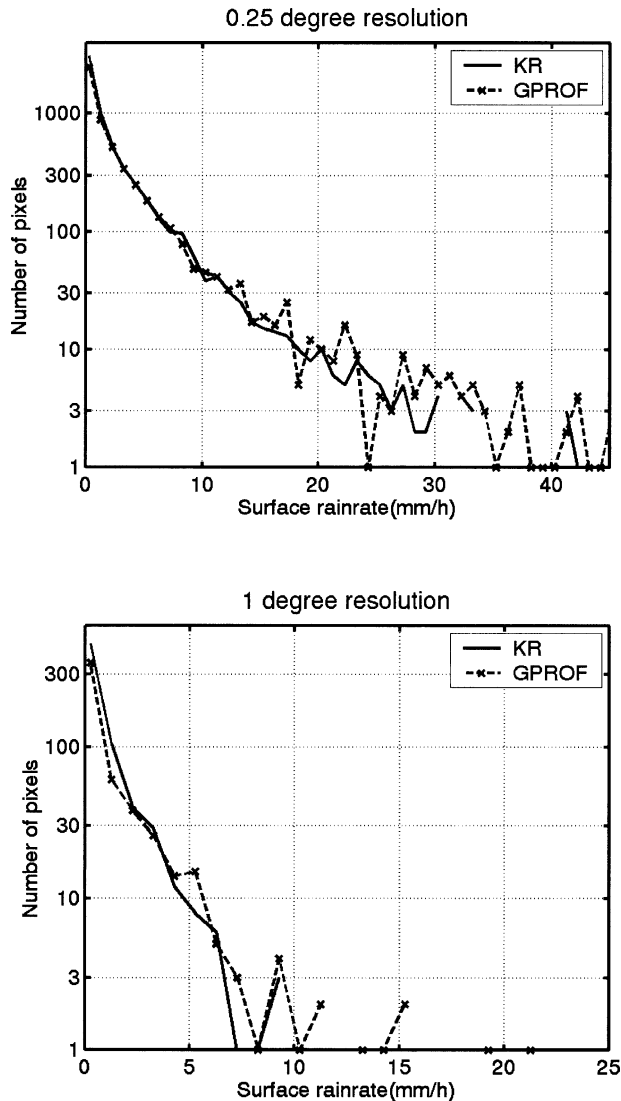


FIG. 3. Histogram of rain rates estimated by the GPROF algorithm and KR.

1 and 13 mm h<sup>-1</sup>. The GPROF algorithm shows more occurrences at heavy rain rates greater than 13 mm h<sup>-1</sup>. This causes the difference in cumulative rainfall distribution for the KR and GPROF algorithm as shown in Fig. 4. In addition, the KR does not show any rainfall occurrences at heavy rain rates greater than 33 mm h<sup>-1</sup> while the GPROF algorithm does. The underestimation (overestimation) of the light (heavy) rainfall is still apparent at 1° resolution when compared with the KR-measured rainfall.

The cumulative rainfall distribution for all KR and GPROF rainy pixels at 0.25° resolution for the 178 overpasses (Fig. 4) suggests that the total rainfall amount retrieved by the GPROF algorithm exceeds that measured by KR by 16% nearly in agreement with Kummerow et al. (2001). Kummerow et al. (2001) showed that the GPROF algorithm underestimated rainfall by

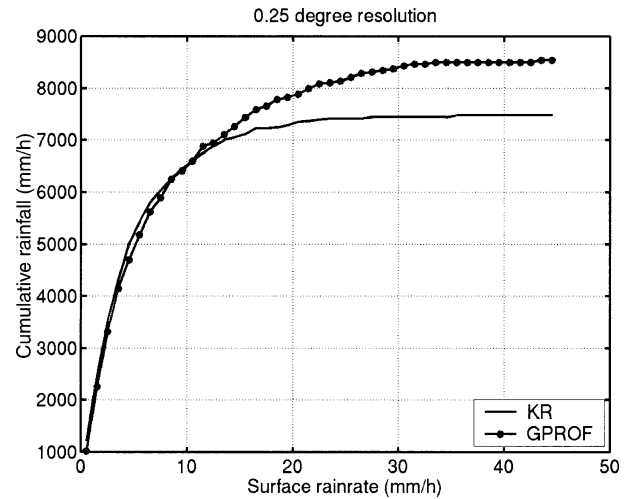


FIG. 4. Cumulative rainfall distributions at 0.25° resolution for the GPROF and KR for 178 overpasses.

32% when compared with rainfall estimated by the rain gauge-adjusted KR data. Kummerow et al. (2001) also predicted that GPROF would overestimate rainfall by approximately 17% when compared with rainfall estimates from the KR calibrated with PR by the University of Washington.

*b. Spatial distribution of rainfall*

To reveal the inconsistencies between the spatial distributions of rainfall from the GPROF algorithm and KR, examples of the spatial variability of two 0.1°-resolution maps on 25 and 28 July 1999 were investigated by Fourier power spectral density (PSD) analysis. The 0.1° resolution is commensurate with the horizontal resolution of 85-GHz channels, which are employed by the GPROF algorithm to determine the horizontal structure in convective systems. The spectral density is defined as the portion of variance explained by a certain wavelength. The PSD of the GPROF-retrieved and KR-estimated rain maps shown in Fig. 5 are shown in Fig. 6.

In this analysis, spectral slope is an indicator of smoothness, while high spectral slopes are characteristic of a smoother structure (Harris and Foufoula-Georgiou 2001). The spectra have been normalized by their respective mean spectral energies. Figure 6 shows that a falloff, showing the transition from low spectral slope to high spectral slope, at small scales (high wavenumbers) around 30–40 km is evident for these two cases in the GPROF-retrieved precipitation field in comparison with the observed KR rainfall field.

To generalize the PSD comparison between the GPROF and KR rain maps, ratios of the normalized PSDs for the GPROF algorithm and KR were calculated at each wavenumber for all 178 cases. The mean and 1-standard-deviation ranges at each wavenumber are shown in Fig. 7. The GPROF-retrieved rain maps show

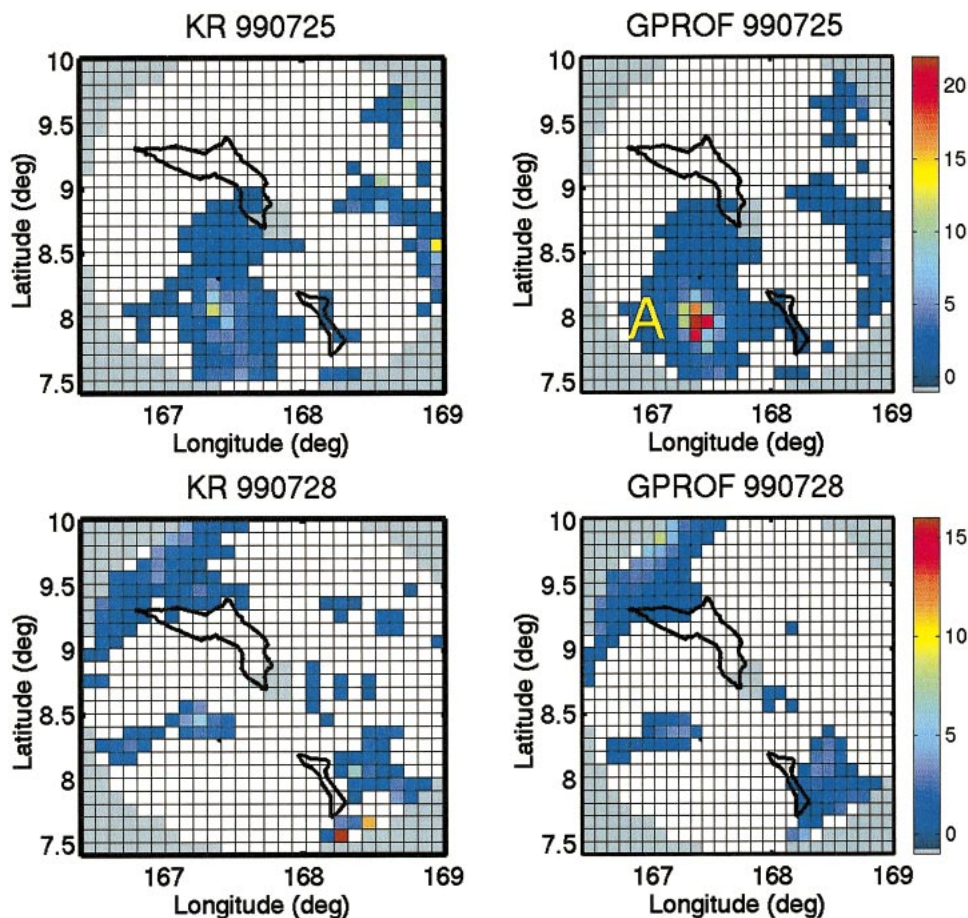


FIG. 5. (left) The KR and (right) the GPROF surface rainfall fields on (top) 25 and (bottom) 28 Jul 1999. Gray boxes correspond to no KR data.

less spatial variability at wavenumbers greater than 0.02 (wavelength  $\sim 50$  km) in the mean demonstrating that GPROF rain areas are smoother and more spatially extensive than those measured by KR. This suggests that the quality of information is generally limited by the lower resolution of the emission channels even though the GPROF products have the same horizontal resolution as the 85-GHz channel.

#### 4. Melting-layer correction

Although melting hydrometeors typically occupy a thin layer of about a 500-m thickness, the microwave absorption and emission by melting layers can account for a significant portion of the emission observed by spaceborne passive radiometers, especially for light rainfall. By neglecting the melting layer, the GPROF algorithm attributes the portion of emission from the melting layer to liquid precipitation. This can result in overestimation of rainfall rates over regions of stratiform precipitation. Recent studies of Schols et al. (1999), Bauer et al. (1999), and Olson et al. (2001a,b)

addressed this issue. It will, no doubt, be included in a subsequent version of the GPROF algorithm.

##### a. Klaassen's melting-layer parameterization

To avoid complex assumptions and computations, this study introduces the parameterization suggested by Klaassen (1990) to insert the melting-layer effect in the current GPROF algorithm. Klaassen's (1990) parameterizations were derived statistically from 50 measurements of the Delft Atmospheric Research Radar (DARR), which is an S-band radar, and attenuation excess simulated by a melting-layer model (Klaassen 1990) at 12, 20, and 30 GHz. Klaassen (1990) shows that the simulated attenuation excess can be estimated from surface measurements of rain intensity or radar reflection.

Using these statistical results, Klaassen (1990) showed that

$$A_e(F) = \alpha R^\beta \quad (1)$$

where  $R$  is the rain rate ( $\text{mm h}^{-1}$ ) measured with melted

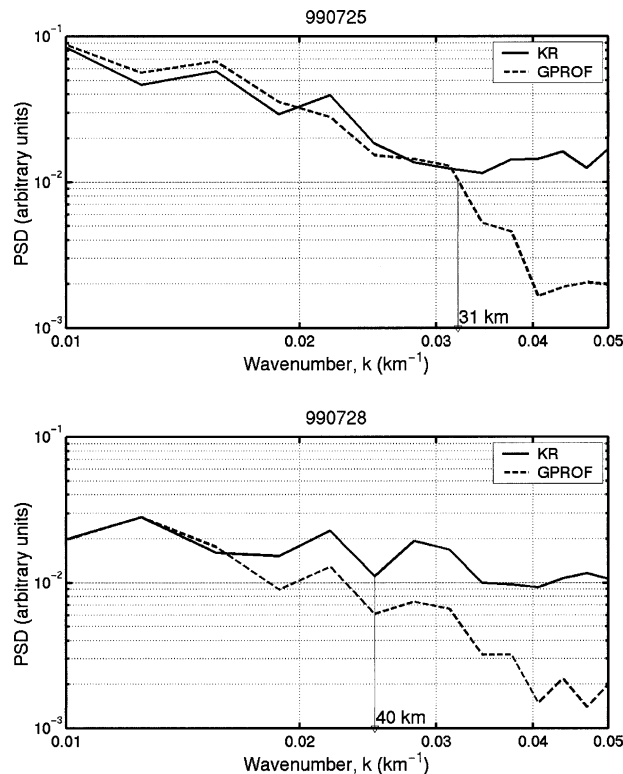


FIG. 6. Spatial Fourier power spectral density normalized to mean spectral density for GPROF-retrieved (dashed lines) and KR-observed (solid lines) surface rain rates at 0.1° resolution on (top) 25 and (bottom) 28 Jul 1999.

water at the surface and  $A_e$  (dB) represents the attenuation excess caused by the absorption and scattering in the melting layer at frequency  $F$  (GHz). The  $\alpha$  and  $\beta$  values for the TMI channels are linearly interpolated for 19.35- and 21.3-GHz frequencies and linearly extrapolated for 10.65- and 37-GHz frequencies, using the values at 12-, 20-, and 30-GHz frequencies given by Klaassen (1990). The estimated constants are given in Table 1.

Because the  $A_e$  is in decibels,

$$A_e = 4.34\Delta k \times \Delta z, \quad (2)$$

where  $\Delta k$  is the excess extinction coefficient and  $\Delta z$  is the depth of a melting layer.

The  $\Delta k$  can be calculated by Eq. (1) and Eq. (2) with rain rates from the GPROF database. The melting-layer effect is considered in the stratiform precipitation profile of the GPROF database by adding  $\Delta k$  to the total absorption coefficient when calculating the emission channels' brightness temperatures for each stratiform precipitation profile. Calculated brightness temperatures at 85 GHz in the GPROF database were excluded in the melting-layer parameterization of this study because this channel is mainly sensitive to ice scattering. The depth of the melting layer is assumed uniform as 500 m based on radar observations over Kwajalein. Because of this

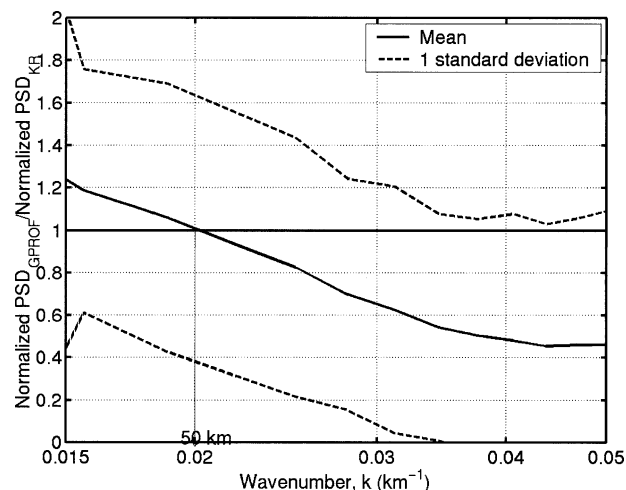


FIG. 7. Ratios of the normalized PSDs for GPROF and KR rain maps. The mean (solid line) and 1 standard deviation (dashed lines) of the ratios for 178 cases are shown. The ratio of 1 is shown as a heavy horizontal line.

increase of absorption coefficient by the melting-layer effect, the modified GPROF database has higher brightness temperatures for given rain-rate profiles, which reduces the stratiform rainfall retrieved from the GPROF algorithm.

*b. Changes of brightness temperatures*

The change in calculated brightness temperature after the melting-layer correction versus surface rain rate is plotted in Fig. 8 for stratiform precipitation from a GCE model simulation for the Tropical Ocean and Global Atmosphere (TOGA) Coupled Ocean–Atmosphere Response Experiment (COARE). The 85-GHz brightness temperature is relatively insensitive to changes in the emission from liquid particles, and so the brightness temperature changes produced by melted snow particles at this frequency are neglected in this study. The result shows that brightness temperature changes produced by including the melting layer increase with rain rate for each frequency. The changes in brightness temperature after the melting-layer correction are as large as 20, 15, 6, and 8 K for a 10 mm h<sup>-1</sup> rain rate at 10.65, 19.35, 21.3, and 37 GHz, respectively. For a given rain rate, the brightness temperature difference gets smaller as

TABLE 1. Statistical relations for the attenuation excess at 12, 20, and 30 GHz given by Klaassen (1990). Constants for TMI channels are estimated by linearly interpolating or extrapolating these given values in this study (\*: interpolated and extrapolated values for TMI channels, ♦: Klaassen's parameters).

Frequency (GHz)	10.65*	12♦	19.35*	20♦	21.3*	30♦	37*
$\alpha$	0.041	0.046	0.069	0.071	0.071	0.073	0.075
$\beta$	0.87	0.85	0.76	0.75	0.74	0.65	0.57

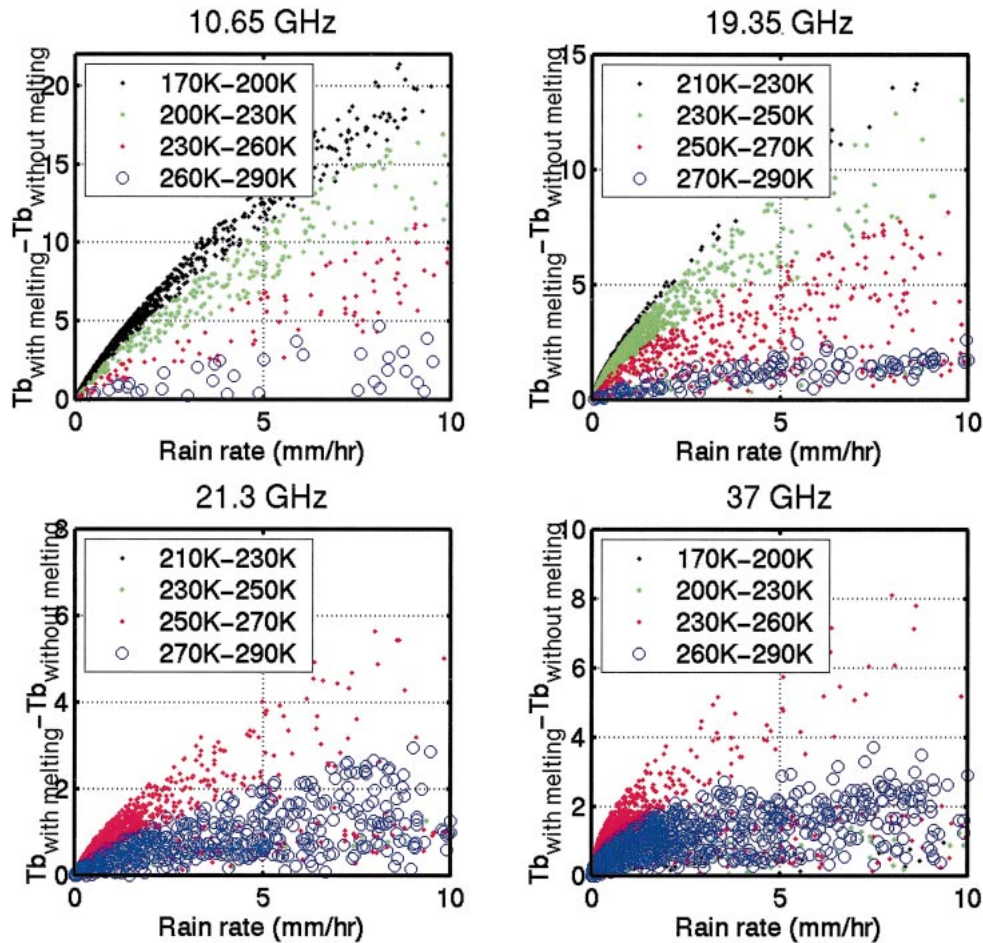


FIG. 8. Changes in brightness temperatures after melting-layer correction vs surface rain rates. The melting-layer correction was applied to simulations of hydrometeor profiles at 1-km resolution from TOGA COARE simulation.

frequency increases, except for 21.3 GHz at which the water vapor absorption band exists.

Even for the same rain rate at a certain frequency, the brightness temperature difference before and after melting-layer correction varies. To show the reason for this, the original brightness temperatures (without the melting-layer effect) are shown in different colors, depending on their scale in Fig. 8. The higher the original brightness temperatures the less they are affected by the melting-layer effect. The brightness temperature at a given rain rate can be different depending on the vertical structure of hydrometeors (e.g., liquid cloud depth, liquid cloud amount). For a hydrometeor profile with a thick cloud, brightness temperatures in emission channels are already high, and so brightness temperature changes produced by melting particles contribute less to the brightness temperature increment.

Results from the comprehensive analysis of the melting layer conducted by Bauer et al. (1999) and Olson et al. (2001a,b) were compared with Klaassen's simplified parameterization. Bauer et al. (1999) showed that

the melting-layer effect was most obvious at 10.7 GHz and diminished at higher frequencies for precipitation over the ocean. They also suggested that the weighted average of the air-ice-in-water and water-in-air-ice mixtures provided better representation of the radiative properties for snow while an ice-in-water mixture provided better results for graupel particles. Olson et al. (2001a) developed a 1D melting-layer model and applied it to the 3D cloud-resolving-model simulated snow and graupel to get the microphysical and radiative properties of melting precipitation. They showed that the increment of upwelling radiances caused by the melting precipitation depends upon the total optical thickness of the cloud and precipitation, as well as the scattering characteristics of mixed phase and ice phase precipitation aloft. Olson et al. (2001b) showed that the optical thickness of cloud and precipitation is relatively low at 10.65 and 19.35 GHz so that the additional absorption/emission by melting precipitation leads to a substantial increase in upwelling radiances.

Figure 11 of Bauer et al. (1999) and Fig. 8 of Olson

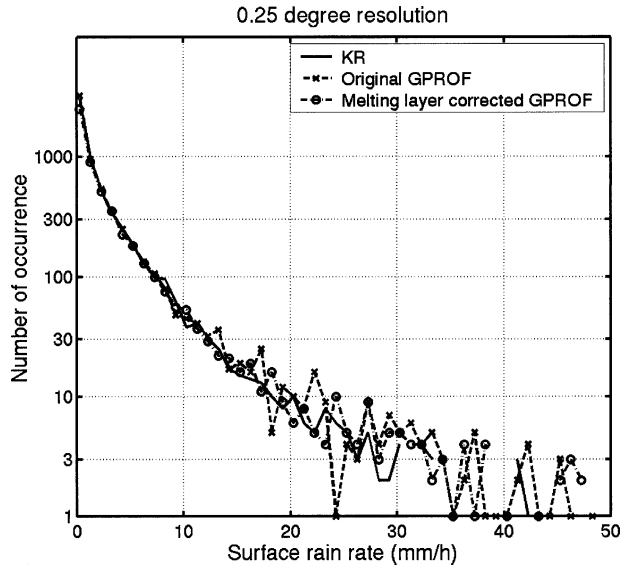


FIG. 9. Histogram showing the frequency of rain-rate occurrence of the original GPROF algorithm, the melting-layer-corrected GPROF, and the KR at 0.25° resolution.

et al. (2001b) are comparable with Fig. 8 of this study. Because the melting-layer correction in this study is applied mainly to melting aggregates in stratiform precipitation, only the results from the weighted average of the air-ice-in-water and water-in-air-ice mixtures, shown in Fig. 11 of Bauer et al. (1999), are applicable for this comparison. The comparison demonstrates that Klaassen's empirical approximation used in this study represents the melting-layer effect to a reasonable degree at frequencies greater than 10 GHz, even though the method is simple and the observations for the parameterization were taken at a different place (the Netherlands) from the tropical oceans.

*c. Changes in rainfall retrievals*

Figure 9 shows the change of rainy pixel numbers at 0.25° resolution for a given rain rate after applying the melting-layer correction to 178 overpasses. Frequencies of rain-rate occurrence at rain rates greater than 10 mm h<sup>-1</sup> are generally reduced and are more consistent to the KR observations. The reason for this decrement is that many pixels in the GPROF database contain a mixture of stratiform and convective precipitation because the database was made by area averaging the GCE model results with resolutions between 1 and 3 km over an approximately 100-km<sup>2</sup> area. In comparison with the original GPROF retrieved rain rates, the melting-layer correction reduced the retrieved rain amount by 7.5% (Fig. 10).

**5. Impact of 85-GHz channels**

*a. Role of the 85-GHz channels*

The emission effect of liquid phase hydrometeors increases brightness temperatures in the low-frequency

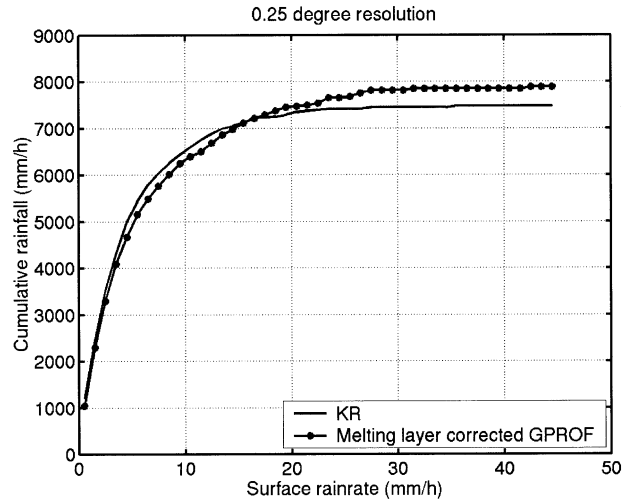


FIG. 10. Cumulative rainfall distributions at 0.25° resolution for the melting-layer-corrected GPROF and KR for 178 overpasses.

channels, and the scattering effect caused by ice phase hydrometeors decreases brightness temperatures in high-frequency channels. The 37-GHz channels are sensitive to both liquid and ice phase hydrometeors while 85-GHz channels are mainly sensitive to ice scattering (Spencer et al. 1989). Therefore, cold brightness temperature at 85-GHz channels play a significant role in matching ice phase hydrometeor profiles in the GPROF database, thus, affecting the rainfall retrievals.

Figure 11 shows brightness temperature at 85 GHz. Note that the region “A” where heavy rainfall was overestimated by the GPROF algorithm, with respect to the KR (Fig. 5b), agrees well with the region with cold brightness temperatures at the 85-GHz frequency. The GPROF algorithm significantly depends on 85-GHz brightness temperatures for heavy rainfall if the 85-GHz brightness temperatures are low.

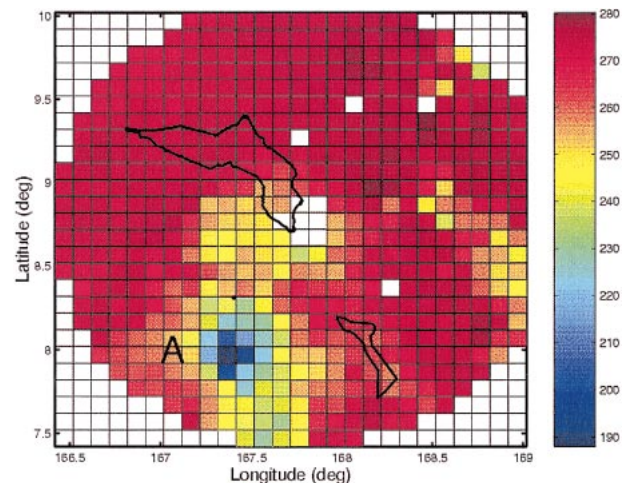


FIG. 11. Vertically polarized brightness temperatures at 85 GHz over KR on 25 Jul 1999.

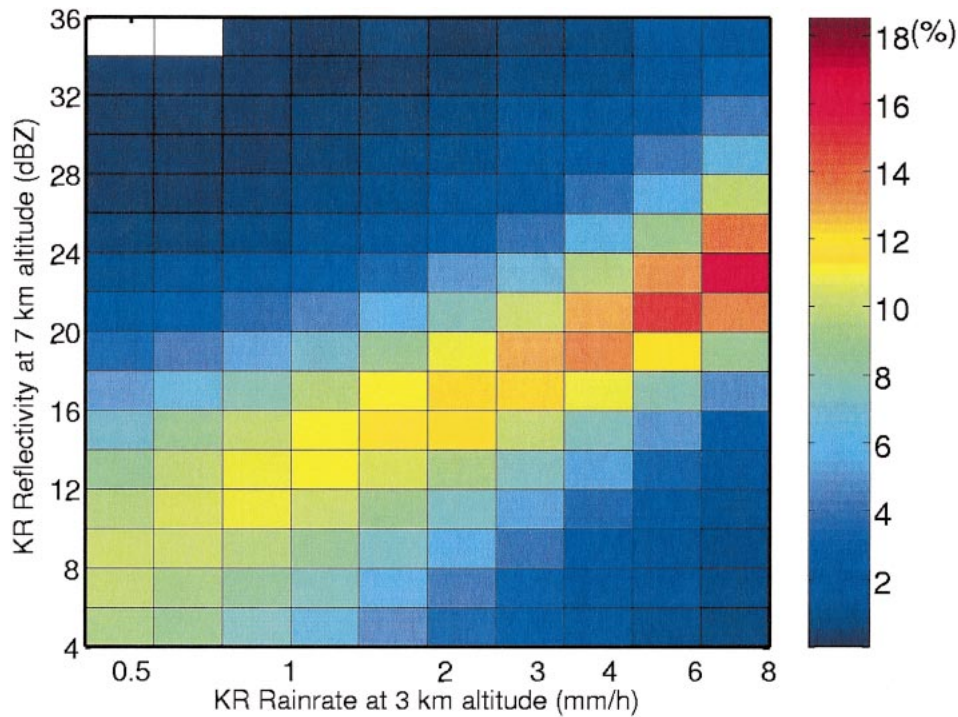


FIG. 12. Percent occurrence of KR rain rates at 3-km altitude for a given KR reflectivity at 7-km altitude for 80 cases.

The upper-level ice amounts are not strongly correlated to rainfall rates near the surface. The ice amounts depend on the characteristics of systems and the stage of the convective systems. For example, a convective system can have significant upper-level ice both in decaying and mature stages while the rainfall intensity is much weaker in the decaying stage than in the mature stage. In addition, wind shear can alter the vertical structure of a convective cloud, which further reduces the correlation between upper-level ice amount and surface rain rate.

Figure 12 shows the percent occurrence of KR rain rates at a 3-km altitude for a given KR reflectivity at a 7-km altitude. The freezing level over the Kwajalein validation site is about 5 km so that the reflectivity at 7 km represents the upper-level ice amount. The result shows that the range of KR rain rates at 3 km for a given 7-km KR reflectivity is large. For example, a reflectivity of 20 dBZ at a 7-km altitude has a range of surface rain rates between 1 and 6 mm h<sup>-1</sup> with a 50% probability. Considering the other sources of uncertainty of the KR mentioned in section 2, the uncertainty inherent in the surface rain rate estimated with the upper-level ice information is even worse. This suggests that using upper-level ice information for rainfall retrieval near the surface contributes little quantitative information over Kwajalein. Rain rates can have large variance for a given 85-GHz radiance observation.

To examine the impact of 85-GHz channels on the rainfall retrievals, this study modifies the GPROF al-

gorithm to neglect 85-GHz brightness temperatures in seeking the best-fit brightness temperature set in the GPROF database for rainfall retrieval. Because of the beam-filling effect on passive microwave rainfall retrievals, we still use 85-GHz channels to estimate convective area fraction.

#### b. Results

Figure 13 shows the change in rainy pixel numbers at each rain rate after neglecting the 85-GHz channels. Rain map comparisons in Figs. 5 (top panels) and 14 show that the general distribution of rainfall and the rainy area has not been changed by neglecting 85-GHz brightness temperatures. Heavy rainfall overestimated by the original GPROF algorithm in convective region "A" in the upper-right panel of Fig. 5 has been reduced after the modification, which is more consistent with the KR observation. This result shows that neglecting ice-scattering information (85 GHz) in finding the best-fit profiles in the GPROF database can reduce the retrieved rainfall amount over the region where the GPROF algorithm overestimated rainfall with respect to the KR-measured rainfall because of strong ice scattering from upper part of the old convective system.

Figure 15 shows the cumulative distribution of surface rainfall retrieved by the revised GPROF algorithm (melting layer corrected and 85-GHz channels' information neglected in the Bayesian calculation except in convective area measurements) for 178 overpass cases.

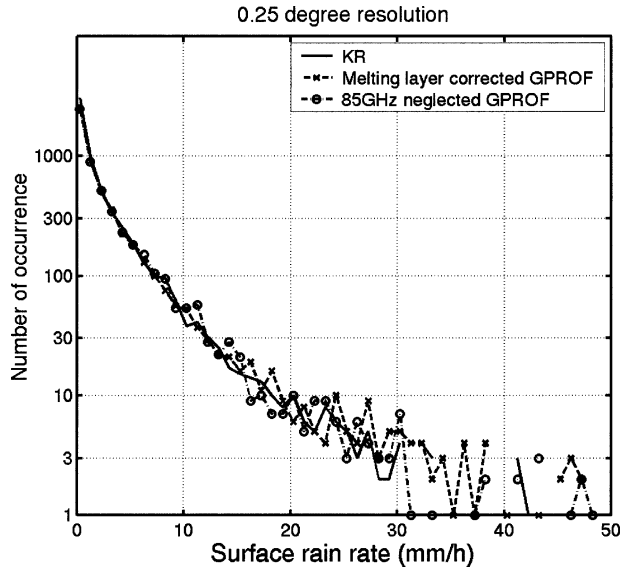


FIG. 13. Histogram comparisons showing the frequency of rain-rate occurrence in the melting-layer-corrected GPROF, the 85-GHz-channel-neglected GPROF, and the KR at 0.25° resolution for a given rain rate.

The rainfall distribution is well matched with KR observations at all range of rain rates. Neglecting 85-GHz brightness temperatures in a melting-layer-corrected GPROF algorithm reduces the retrieved rain amount by 3.5%. When compared with the original GPROF algorithm–retrieved rain amount, the GPROF rain rate estimates that include a melting-layer correction and neglect the 85-GHz brightness temperatures reduce the retrieved rain amount by 18%. When compared with the KR-measured rain amount, this modified GPROF algorithm overestimates rain amount by 1%.

Neglecting 85-GHz brightness temperatures may not be generalized for all kinds of precipitation systems and for other geophysical locations. However, results of this sensitivity test suggest that the way to employ 85-GHz observations in the GPROF algorithm (version 5) for surface rainfall retrievals may be a significant error source, especially over regions with a large area convective systems where strong ice scattering exists. The current a priori database does not properly represent the actual variety in hydrometeor profiles, and a future version of the GPROF algorithm may have a better performance as the database is updated. Results also suggest that an effort to improve the database will be more important for land algorithms, which depend exclusively upon the 85-GHz brightness temperature to retrieve hydrometeor profiles.

**6. Summary and conclusions**

Providing high-resolution rainfall products for mesoscale atmospheric research has become a concern of the satellite remote sensing community, especially over

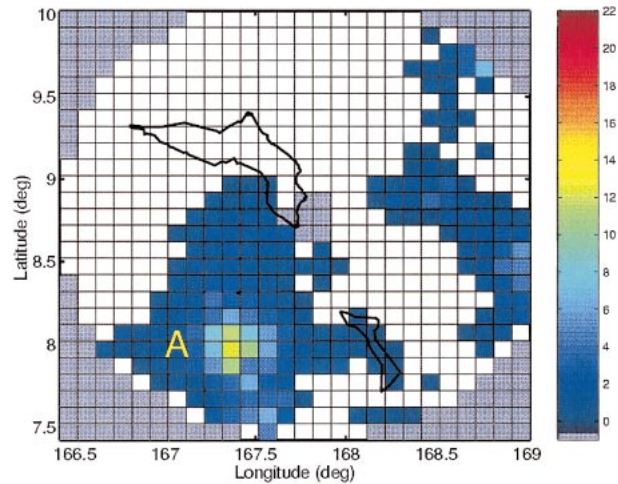


FIG. 14. Surface rainfall map for 25 Jul 1999 after neglecting the 85-GHz brightness. Compare the region designated “A” with that shown in the upper-right panel of Fig. 5.

oceans where ground-based observations are not generally available. This study attempted to evaluate the ability of the GPROF algorithm to retrieve rainfall at resolutions down to 0.25° by comparing GPROF surface rainfall retrievals with KR observations for 178 overpass cases between 1998 and 1999.

The GPROF algorithm overestimated rainfall by 16% when compared with the KR observations. Results showed that the GPROF algorithm overestimated heavy rainfall at 0.25° and 1.0° resolutions with respect to the KR. Sensitivity of GPROF surface rainfall retrievals to the melting-layer effect and the impact of 85-GHz channels were examined to reduce biases of the retrieved rainfall with respect to the KR-estimated rainfall.

Power spectral density comparisons between GPROF

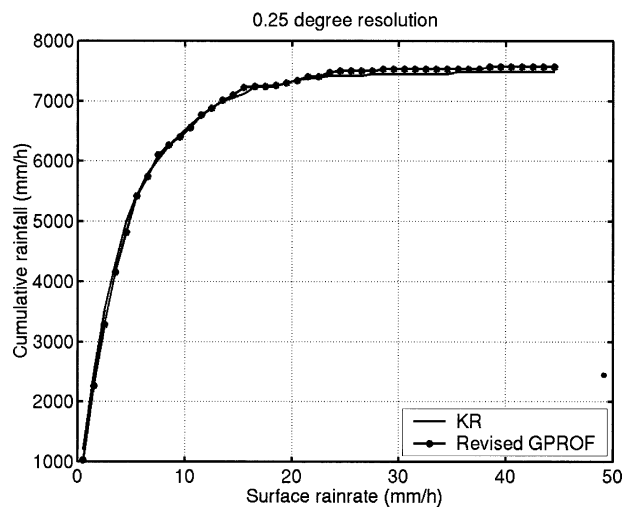


FIG. 15. Cumulative rainfall distributions of the KR and the melting-layer-corrected and 85-GHz-channel-neglected (except for the calculation of convective area fraction) GPROF algorithm at 0.25° resolution.

and KR rain maps at 0.1° resolution show that GPROF-retrieved rain maps are less spatially variable at wavelengths less than 50 km in the mean, suggesting that the GPROF rainy areas are smoother and more spatially extensive than those observed by the KR.

This study employed the oceanic GPROF algorithm over the whole Kwajalein validation site. The current GPROF algorithm neglects the melting layer in stratiform precipitation. This study employs Klaassen's (1990) melting-layer parameterization in the GPROF algorithm. This empirical parameterization is simpler than a realistic melting-layer model, such as that of Bauer et al. (1999) and Olson et al. (2001a,b), but resulted in the same amount of brightness temperature change after the melting-layer correction. The melting-layer correction reduced the GPROF-retrieved rainfall amount by 7.5% in this study (Fig. 10).

To examine the effect of uncertainty caused by the poor correlation between upper-level ice amount and surface rainfall, this study only estimated the convective area fraction from 85-GHz brightness temperatures and neglected 85-GHz brightness temperatures in the GPROF database used to derive the rainfall retrieval. Neglecting ice-scattering information (85 GHz) in finding the best-fit profiles in the GPROF database improved the surface rainfall retrievals over the region where ice scattering was significant in the old convective system and reduced the rain amount by 3.5%.

The cumulative distribution of surface rainfall retrieved by the revised GPROF algorithm (the melting layer is corrected and 85-GHz channels' information neglected in the Bayesian calculation, except in convective area measurements) for 178 overpass cases shows that the rainfall distribution is generally well matched with KR observations at all ranges of rain rates (Fig. 15). For the 178 overpasses used in this study the total rainfall amount retrieved by the revised GPROF algorithm overestimated rainfall by 1% with respect to that measured by the KR.

*Acknowledgments.* This work has been supported by NASA Grant NAG5-9668 and NCC-5-584, and by Grant NAG5-13654. We thank Dr. Ramesh Kakar for his interest in this study. We also thank Dr. W. Olson and Dr. C. Kummerow, and G. Dargaud for the supporting computer system to run the GPROF algorithm and providing answers to our questions on the GPROF algorithm. We also thank S. Brodzik for helping us to analyze the KR data. We are also grateful to Professors S. Yuter, C. Bretherton, M. Baker, and C. Schumacher; and to Dr. G. Skofronick-Jackson, Dr. M. Grecu, and three anonymous reviewers for their constructive comments, which helped us to improve this paper.

#### REFERENCES

- Adler, R. F., and A. J. Negri, 1988: A satellite infrared technique to estimate tropical convective and stratiform rainfall. *J. Appl. Meteor.*, **27**, 30–51.
- Bauer, P., L. Schanz, and L. Roberti, 1998: Correction of three-dimensional effects for passive microwave remote sensing of convective clouds. *J. Appl. Meteor.*, **37**, 1619–1632.
- , J. P. V. Poiares Baptista, and M. De Iulius, 1999: The effect of the melting layer on the microwave emission of clouds over the ocean. *J. Atmos. Sci.*, **56**, 852–867.
- Harris, D., and E. Foufoula-Georgio, 2001: Subgrid variability and stochastic down scaling of modeled clouds: Effects on radiative transfer computations for rainfall retrieval. *J. Geophys. Res.*, **106**, 10 349–10 362.
- Hartman, D. L., 1994: *Global Physical Climatology*. Academic Press, 411 pp.
- Houze, R. A., Jr., S. Brodzik, C. Schumacher, S. E. Yuter, and C. R. Williams, 2004: Uncertainties in oceanic radar rain maps at Kwajalein and implications for satellite validation. *J. Appl. Meteor.*, in press.
- Joss, J., and Coauthors, 1998: *Operational Use of Radar for Precipitation Measurements in Switzerland*. vdf Hochschulverlag AG an der ETH (University Press of the Swiss Federal Institute of Technology), 108 pp.
- Klaassen, W., 1990: Attenuation and reflection of radio waves by a melting layer of precipitation. *Proc. IEEE*, **137**, 39–44.
- Kozu, T., and Coauthors, 2001: Development of precipitation radar onboard the tropical rainfall measuring mission satellite. *IEEE Geosci. Remote Sens.*, **39**, 102–116.
- Kummerow, C., 1998: Beamfilling errors in passive microwave rainfall retrievals. *J. Appl. Meteor.*, **37**, 356–369.
- , and J. A. Weinman, 1988: Radiative properties of deformed hydrometeors for commonly used passive microwave frequencies. *IEEE Trans. Geosci. Remote Sens.*, **26**, 629–638.
- , W. Barnes, T. Kozu, J. Shiue, and J. Simpson, 1998: The Tropical Rainfall Measuring Mission (TRMM) sensor package. *J. Atmos. Oceanic Technol.*, **15**, 808–816.
- , and Coauthors, 2000: The status of the Tropical Rainfall Measuring Mission (TRMM) after two years in orbit. *J. Appl. Meteor.*, **39**, 1965–1982.
- , and Coauthors, 2001: The evolution of the Goddard profiling algorithm (GPROF) for rainfall estimation from passive microwave sensors. *J. Appl. Meteor.*, **40**, 1801–1820.
- Olson, W. S., P. Bauer, C. Kummerow, Y. Hong, and W. K. Tao, 2001a: A melting layer model for passive/active microwave remote sensing applications. Part I: Model formulation and comparison with observations. *J. Appl. Meteor.*, **40**, 1145–1163.
- , —, —, and —, 2001b: A melting layer model for passive/active microwave remote sensing applications. Part II: Simulation of TRMM observations. *J. Appl. Meteor.*, **40**, 1164–1179.
- , Y. Hong, C. D. Kummerow, and J. Turk, 2001c: A texture-polarization method for estimating convective-stratiform precipitation area coverage from passive microwave radiometer data. *J. Appl. Meteor.*, **40**, 1577–1591.
- Petty, G. W., and K. B. Katsaros, 1990: Precipitation observed over the South China Sea by the Nimbus-7 scanning multichannel microwave radiometer during Winter MONEX. *J. Appl. Meteor.*, **29**, 273–287.
- Schols, J. L., J. A. Weinman, G. D. Alexander, R. E. Stewart, L. J. Angus, and A. C. L. Lee, 1999: Microwave properties of frozen precipitation around a North Atlantic cyclone. *J. Appl. Meteor.*, **38**, 29–43.
- Schumacher, C., and R. Houze, 2000: Comparison of radar data from the TRMM satellite and Kwajalein oceanic validation site. *J. Appl. Meteor.*, **39**, 2151–2164.
- , and R. A. Houze Jr., 2003a: Stratiform rain in the Tropics as seen by the TRMM precipitation radar. *J. Climate*, **16**, 1739–1756.
- , and —, 2003b: The TRMM precipitation radar's view of shallow, isolated rain. *J. Appl. Meteor.*, **42**, 1519–1524.
- Sellers, W. D., 1965: *Physical Climatology*. University of Chicago Press, 272 pp.
- Smith, E. A., and A. Mugnai, 1988: Radiative transfer to space

- through a precipitating cloud at multiple microwave frequencies. Part II: Results and analysis. *J. Appl. Meteor.*, **27**, 1074–1091.
- , ———, H. J. Cooper, G. J. Tripoli, and X. Xiang, 1992: Foundations for statistical-physical precipitation retrieval from passive microwave satellite measurements. Part I: Brightness-temperature properties of a time-dependent cloud-radiation model. *J. Appl. Meteor.*, **31**, 506–531.
- Spencer, R. W., H. M. Goodman, and R. E. Hood, 1989: Precipitation retrieval over land and ocean with SSM/I: Identification and characteristics of the scattering signal. *J. Atmos. Oceanic Technol.*, **6**, 254–273.
- Weinman, J. A., and P. J. Guetter, 1977: Determination of rainfall distributions from microwave radiation measured by the Nimbus-6 ESMR. *J. Appl. Meteor.*, **16**, 437–442.
- Wilheit, T. T., T. C. Chang, M. S. V. Rao, E. B. Rodgers, and J. S. Theon, 1977: A satellite technique for quantitatively mapping rainfall rates over the ocean. *J. Appl. Meteor.*, **16**, 551–560.
- Wu, R., and J. A. Weinman, 1984: Microwave radiances from precipitating clouds containing aspherical ice, combined phase and liquid hydrometeors. *J. Geophys. Res.*, **89**, 7170–7178.